Werk

Jahr: 1988
Kollektion: fid.geo
Signatur: 8 Z NAT 2148:62
Digitalisiert: Niedersächsische Staats- und Universitätsbibliothek Göttingen
Werk Id: PPN1015067948_0062
PURL: http://resolver.sub.uni-goettingen.de/purl?PPN1015067948_0062

LOG Id: LOG_0030
LOG Titel: The upper-mantle discontinuities underneath the GRF array from P-to-S converted phases
LOG Typ: article

Übergeordnetes Werk

Werk Id: PPN1015067948
PURL: http://resolver.sub.uni-goettingen.de/purl?PPN1015067948
OPAC: http://opac.sub.uni-goettingen.de/DB=1/PPN?PPN=1015067948

Contact

Niedersächsische Staats- und Universitätsbibliothek Göttingen
Georg-August-Universität Göttingen
Platz der Göttinger Sieben 1
37073 Göttingen
Germany
Email: gdz@sub.uni-goettingen.de

J Geophys (1988) 62:138–147

Journal of Geophysics

The upper-mantle discontinuities underneath the GRF array from *P*-to-*S* converted phases

R. Kind [1] **and L.P. Vinnik** [2]

[1] Seismologisches Zentralobservatorium, Krankenhausstrasse 1, 8520 Erlangen, Federal Republic of Germany
[2] Institute of the Physics of the Earth, Academy of Sciences of the USSR, Moscow, USSR

Abstract. A data-processing method is applied which includes a rotation of the three components, normalization and delay-and-sum of broadband records of earthquakes from a large distance and azimuth distribution, recorded at a single station (or an array). Clear *P*-to-*S* converted phases at the mantle discontinuities are observed in the Gräfenberg records, after this data processing. Theoretical seismograms are computed for the PREM model and processed in the same way as the observed data. A comparison with the data shows that the depth interval between the two discontinuities in the mantle transition zone (those at 400 and 670 km depth in PREM) is around 240 km. The 670-km discontinuity is sharper than the 400-km discontinuity and is comparable in sharpness with the crust-mantle transition, as far as it is possible to judge from the broadband data used. There are indications of pronounced lateral heterogeneity of the 400-km transition, underneath GRF. We have also observed converted and multiply reflected shear waves in the crust, which set sensitive limits to the average crustal model underneath the array. These data suggest that the velocity jump at the Moho is smaller than indicated by refraction studies.

Key words: Upper-mantle transition zones – *P*-to-*S* conversions – Theoretical seismograms

Introduction

The bulk of the presently available seismic data on the structure of the upper-mantle discontinuities comes from observations of refracted and overcritically reflected body waves. The errors in the depth determinations of the mantle discontinuities from these data can reach a few tens of kilometres. Similarly, refracted waves are rather insensitive to the sharpness of a discontinuity. A poor lateral resolution is another deficiency of the method: refracted and overcritically reflected waves penetrating to a depth of 650 km return to the Earth's surface at a distance of about 3000 km from the epicentre, thus averaging the effects of lateral variations in the deep structure of the Earth. On the other hand, detailed and accurate seismic data on the properties of these discontinuities (depth, sharpness, lateral variations) are necessary for constraining models of mantle composition and dynamics (e.g. see Jeanloz and Thompson, 1983). Several attempts have been made to use converted phases to study the upper-mantle structure. For example, Paulssen (1985) has tried to detect converted shear waves in the *P* coda. Faber and Müller (1984) have observed long-period forerunners of *S*, converted at upper-mantle discontinuities.

To meet demands for higher resolution and accuracy, a technique of using teleseismic waves converted from *P* to *SV* at the upper-mantle discontinuities was developed (Vinnik, 1977). The converted phases are recorded in the *P*-wave coda with amplitudes of the order of a few percent of the *P*-wave amplitude. To detect such weak phases a special signal-processing procedure is required. This procedure is, in principle, a delay-and-sum method similar to the conventional velocity filtering; but instead of an array of seismic receivers, use is made of an array of sources. The technique has been applied so far to the records of a few seismograph stations (only one of them digital), and converted phases corresponding to the mantle discontinuities were consistently observed (Vinnik et al., 1983).

In this paper we present results of the application of a similar approach to the data of the Gräfenberg array. The main advantage of the Gräfenberg records lies in their broadband frequency content which makes them ideally suited for this purpose. The inversion of the observations for mantle structure has been carried out by generating synthetic records for a number of models, passing the synthetics through the same signal-processing procedure as the real seismograms and comparing the results of observation and modelling. The conclusions thus derived are summarized and discussed in the last section of the paper.

A method to detect converted phases

The method of detecting converted phases was described earlier (Vinnik 1977; Vinnik et al. 1983). We repeat these descriptions here with minor modifications. We consider the *P* wave of a distant earthquake converted to *SV* on the receiver side of the wave path and recorded by a three-component seismograph set (Fig. 1).

The *P* wave and noise with the same angle of incidence as the *P* wave are suppressed by projecting the record on the *H* axis which is perpendicular to the principal direction of the *P*-wave particle motion *L* and lies in the vertical plane (Fig. 1). In Fig. 1 the direction *L* is shown coinciding with that of the *P*-wave ray path, although in reality they are somewhat different. The angle *e* between *L* and the

Offprint requests to: R. Kind

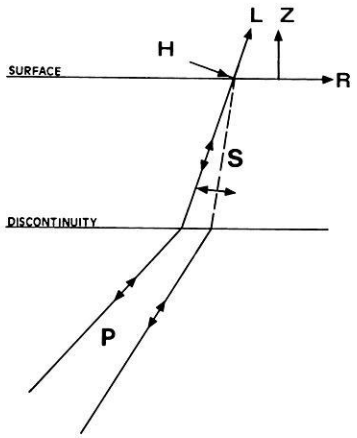

Fig. 1. Sketch of the coordinate systems used and of the ray path of a phase converted at an upper-mantle discontinuity

radial direction R can be found from the expression (Vinnik et al. 1983)

$$e=\tan^{-1}[\langle R(t)\,Z(t)\rangle/(\lambda-\langle Z^2(t)\rangle)].$$

$R(t)$ and $Z(t)$ are ground-motion components which correspond to the direction R and the vertical direction Z, respectively; t is time; $\langle\ \rangle$ denotes averaging over the time interval from the beginning to the end of the main P-wave train; λ is the biggest root of the equation

$$(\langle Z^2(t)\rangle-\lambda)(\langle R^2(t)\rangle-\lambda)-\langle R(t)\,Z(t)\rangle^2=0.$$

To detect the converted phases which are hidden in the P-wave coda, the H-component records of many seismic events should be stacked. To facilitate stacking, the differences between the records arising from differences in the magnitudes and source functions of various events are reduced by transforming the records into a standard form, which is the normalized crosscorrelation function of the H and L components. The standardized $\hat{H}$ component can be expressed as

$$\hat{H}(t)=\int_{t_1}^{t_2} H(t+\tau)\,L(\tau)\,d\tau \Big/ \int_{t_1}^{t_2}[L(\tau)]^2\,d\tau$$

where t is now the delay time between H and L, t_1 and t_2 correspond to the first-arrival time and the end of the main P-wave train, respectively. A similar matched filter procedure with the autocorrelation of the P-wave signal as normalizing function was used by Schlittenhardt (1986) to determine the PcP/P amplitude ratio.

Assuming that the form of the converted wave train is similar to that of the P-wave train, the maximum value of the function $\hat{H}$ is equal to the amplitude ratio Ps/P; the value of t which corresponds to this maximum is equal to the time interval between the Ps and P arrivals. This time interval is given by

$$t_{Ps}=\int_{r_c}^{r_0}(v_s^{-2}-p^2r^{-2})^{1/2}\,dr-\int_{r_c}^{r_0}(v_p^{-2}-p^2r^{-2})^{1/2}\,dr$$

where r is the radial distance, r_c is the location of the interface of conversion and r_0 is the earth's radius. $v_p(r)$ and $v_s(r)$ are the P and S velocities and p is the ray parameter

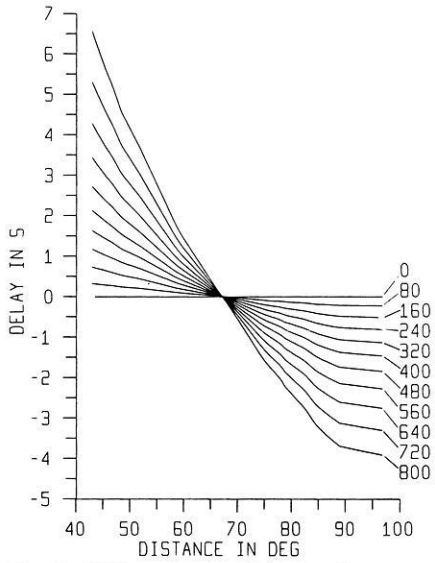

Fig. 2. Difference travel times of a converted phase and the P time as a function of distance and depth of an assumed discontinuity, normalized by the difference time at 67°. The numbers at the right are the depths of the discontinuity in km

of the P wave. This equation was derived on the assumption that the ray parameter values are the same for P and Ps, while in reality they are somewhat different. The exact values of t_{Ps} are somewhat lower than these estimates. For conversions in the upper mantle, the difference is of the order of a fraction of a second. Such accuracy is sufficient for estimating relative time delays for the phases corresponding to the same conversion depth and varying epicentral distances.

To enhance the waves converted at depth h and simultaneously reduce all other wave types, the $\hat{H}$ components of many seismic events in a broad epicentral distance range are delayed and summed. The delay $\delta t_i(h)$ can be expressed as

$$\delta t_i=t^i_{Ps}(h)-t^0_{Ps}(h)$$

where $t^i_{Ps}(h)$ is calculated for the slowness p (or the corresponding distance) of the P wave of the i-th event, and $t^0_{Ps}(h)$ is calculated for a reference value of p which was taken equal to 6.4 s/degree (or 67° distance). The dependence of δt_i on p or epicentral distance is illustrated by Fig. 2. The summed records are normalized by dividing the amplitude by the number of events. The summation is performed for a number of trial conversion depths ("phasing depths"). The procedure is similar to the conventional array beam forming, but instead of an array of seismic receivers we use an array of sources; the apparent velocity and azimuth as unknown parameters are replaced by the phasing depth. In the case of the conventional beam forming, the best slowness and azimuth values of a seismic wave can be obtained from a comparison of beam amplitudes. Similarly, a rough estimate of the depth of conversion can be obtained from a comparison of amplitudes corresponding to the different phasing depths. The actual depth of conversion can be found much more accurately from the time delay of the converted phase. The proximity of both depth estimates implies that the phase is a true converted wave rather than an artefact of processing.

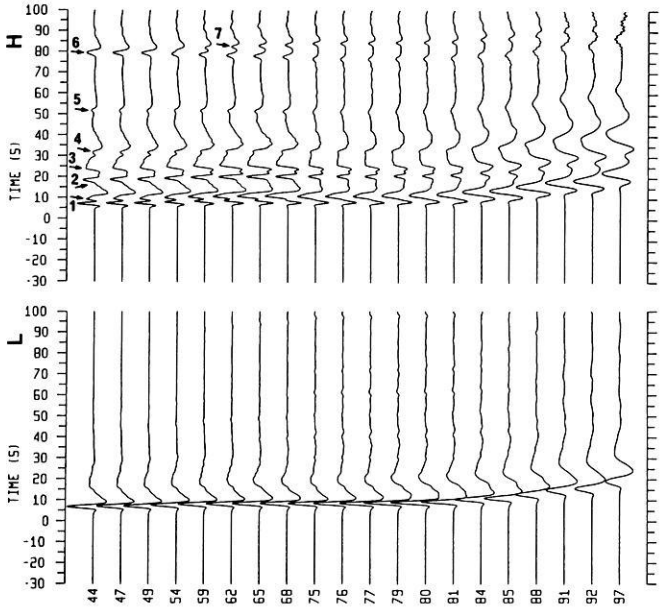

Fig. 3. Theoretical H and L components for the PREM model. All traces are normalized independently. Phase 1 is the conversion at the Moho, phase 2 is the PS multiple in the crust, phase 3 is the SS multiple in the crust, phase 4 is the conversion at 220 km, phase 5 is the conversion at 400 km, phase 6 is the conversion at 670 km and phase 7 is the PS multiple at the 200-km discontinuity. The rise time of the theoretical source function is 2.5 s

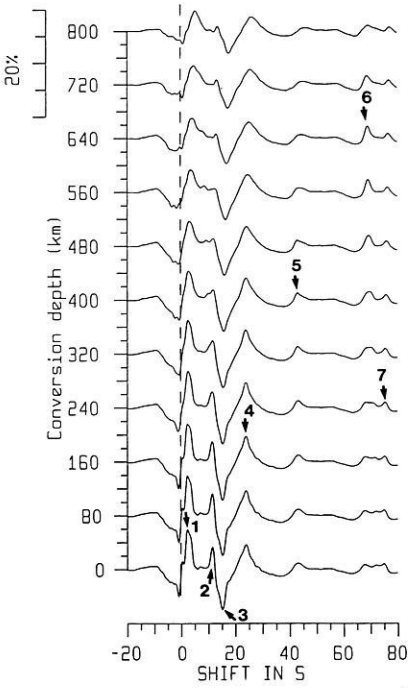

Fig. 4. Delayed and summed theoretical $\hat{H}$ components from Fig. 3. The numbers refer to the same phases as in Fig. 3. It can clearly be seen that, for example, the signal improvement for the conversion at the 670-km discontinuity is best for a trial conversion depth close to 670 km. The amplitude scale is the ratio Ps/P in percent. The same scale is given in Figs. 7–10

Computation of theoretical seismograms

The interpretation of the observed converted phases is carried out with the aid of theoretical seismograms. The version of the reflectivity method developed by Kind (1985) is used. This method provides complete body-wave seismograms for a buried source and different structures at source and receiver sides. We have used a dislocation point source buried at 750 km depth. This large source depth makes sure that there is no interference of the P-wave group with depth phases or a complicated near-source structure. Near-source effects in the observed data are reduced because of the summation of events from different regions and differnt source dephts. We have avoided this complication in the theoretical seismograms by using a deep source and a smooth mantle at the source side. The complete response of the structure under the station, including effects of the free surface, are taken into account. A strike-slip source was used and a profile at 45° azimuth was computed. The same source orientation was used for all computed seismogram sections. The source-time function is a smooth ramp function in moment with the rise time as a parameter. The same broadband displacement filter which has been used to process the observed data has also been applied to the theoretical data. The distances have been chosen to cover the same range as the observed data; their spacing is also similar.

Figure 3 shows theoretical L and H components for the PREM mantle at the receiver side (Dziewonski and Anderson, 1981). The Jeffreys-Bullen model is used at the source side, because we wanted a smooth model near the source. The crustal layers of PREM have been replaced by a model more appropriate for Gräfenberg (Table 2, model B). A fixed angle of 25° was used for the rotation of the coordinate system for all distances. We have, therefore, still some P energy on the H component. The theoretical seismograms in Fig. 3 are proportional to ground displacement. The rise time is 2.5 s. The H component is much more complicated than the L component. This is due to several converted or multiply reflected phases arriving as shear waves the station. The conversions at the Moho and at the 220-, 400- and 670-km discontinuities in PREM, and a few multiples, are marked in Fig. 3. All these phases have been identified by experiments with theoretical seismograms. The SV phases are very weak (a few percent of the P wave). It is understandable that such weak phases are difficult to detect directly in seismic records. Signal-generated noise in the real earth is easily larger than these weak conversions. The conversions have, however, a big advantage; they correlate, whereas the noise does not correlate over many records.

The theoretical seismograms in Fig. 3 have been processed exactly in the same way as the observed ones, for direct comparison with the observed data, using the method described in the previous section. The results of this processing procedure are shown in Fig. 4. The rise time of 2.5 s in Fig. 3 was used in order to reduce some high-frequency numerical noise. A rise time of 2.0 s in Fig. 4 is used because the high-frequency noise here is reduced by the summation. The conversions at the mantle discontinuities have their largest amplitudes at their appropriate conversion depths. The conversions or multiples in the crust have their largest amplitudes at zero or a small conversion depth (meaning zero or small delays for the summation). The conversion in PREM at 220 km interferes with the crustal multiples and is therefore difficult to see.

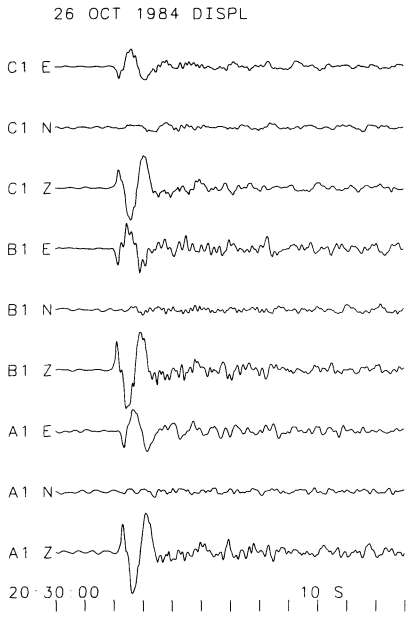

Fig. 5. Three-component displacement records of event 28, Table 1. The azimuth of this event is 80°. The E and N components are, therefore, practically the radial and transverse components, respectively

Observation of converted phases

The first step in processing the records of the GRF array was the summation of the vertical, radial and transverse components of its three 3-component stations. This has been done in order to improve the signal-to-noise ratio by suppressing microseisms and the incoherent signal-generated noise. The summed records were filtered with three different filters. The transfer function of the first filter is flat with respect to ground displacement in the frequency range between 0.05 and 5.00 Hz. The teleseismic P signals at the output of this filter usually contain frequencies between, approximately, 0.05 and 1.00 Hz. In order to analyse a possible frequency dependence in the observed wave field, two narrow band-pass filters were used. The cut-off frequencies were 0.065 and 0.130 Hz for the second filter and 0.125 and 0.250 Hz for the third one. The dominant periods at the outputs of the second and third filter were around 10 and 5 s, respectively. The subsequent processing was performed as described earlier.

The angles of incidence computed with the method described earlier are normal. Liu and Kind (1986) have observed unusually steep angles of incidence in particle-motion diagrams of short-period P waves at GRF. The reason for this is extremely low-velocity, but thin, sedimentary layers underneath the Jurassic layer (Frank Krüger, personal communication).

Figure 5 shows the displacement data of the three-component stations for event 28 (Table 1). The back azimuth of the event is 80°, so that the E component is practically the radial component and the N component corresponds to the transverse component. Figure 6 shows examples of the vertical component of some of the events used in the three frequency bands.

The list of processed events is given in Table 1. Criteria for event selection were: large amplitude of P relative to microseismic noise, relatively short duration of the main P-wave train (usually not more than 40 s), absence of visible secondary phases like pP or sP in the critical part of coda. The length of the time windows of the P wave used varies between 30 and 50 s. Shallow or deep events are useful; intermediate-depth events are less suitable. Some events of Table 1 could satisfy the quality requirements only in one or two frequency bands. In the first (broad) and second (around 0.1 Hz) frequency bands, the number of usable records was fairly large (33 and 32, respectively). In the third frequency band (around 0.2 Hz), it was much lower (15). Many "good" events can be found in the distance range between 70° and 100° but, unfortunately, there are not enough events in the range between 35° and 60°. Representative samples of $\hat{H}(t)$ are shown in Fig. 7. The stacked records are presented in Fig. 8.

A visual inspection of stacked records in Fig. 8 leads to the following observations. In the first (broad) frequency range, the initial part of the stacked records is dominated by strong crustal converted and multiple reflected phases. The amplitude in the first 30 s decreases with growing conversion depth. In the time interval around 45 s at shallow conversion depths one can see a bay-like phase with a duration around 20 s. As the conversion depth comes closer to 400 km, the amplitude of this phase increases due to a contribution from higher frequencies. As the depth grows further, the amplitude decreases. The times around 45 s correspond to depths of conversion around 400 km; the amplitude distribution in the time interval around 45 s fits this depth perfectly. Thus, the phase with the time around 45 s is, most likely, formed by conversion at 400 km depth.

In the time interval around 68 s one can see a second clear mantle phase. As the depth of conversion comes to 640 km, this phase changes its shape from a bay-like feature to a nearly perfect triangle. This is caused by the improved correlation, especially at higher frequencies. This shape deteriorates as the depth exceeds 640 km. The times around 68 s correspond to depths of conversion around 640 km and thus, again, the amplitude versus depth distribution and the time are in good agreement with each other. We observe that the converted phase which is related to conversion at 640 km depth has higher frequencies than the first mantle phase.

The wave field in the second frequency band (0.1 Hz), like that in the broad band, is dominated by the crustal phases (first 30 s), the phase converted near 400 km depth and the phase converted near 640 km depth. The amplitude of the second mantle phase is notably larger. The value t_{Ps} of a converted phase corresponds to the (positive) maximum of $\hat{H}(t)$. These values are 45.0 s and 68.2 s for the first and second mantle phase, respectively (they correspond to a reference slowness of 6.4 s/degree or 67° distance.

The third frequency band (0.2 Hz) is noisier than the other two. Nevertheless, both mantle phases are seen, especially the second one (at 68.2 s). Their t_{Ps} values coincide with those found in the first and second frequency bands. The amplitude of the second phase in the 0.2-Hz frequency band is nearly 70% of that in the 0.1-Hz band.

To test the stability of the observed wave field and the accuracy of our estimates of the parameters, we have performed a series of numerical experiments. In these experiments, the available $\hat{H}$-component records were divided into groups and the records of each group were stacked separately. In the first experiment, the events were divided into two groups so that the epicentral distance range and

Table 1. List of events used in this study

No	Day	Month	Year	Origin time	Latitude	Longitude	Depth	Magnitude	Distance	Azimuth
01	09	03	1977	14 27 56.2	41.7N	131.1E	556	5.9	74.8	42
02	04	09	1977	15 40 55.0	51.1N	178.4E	20	5.6	79.0	8
03	16	08	1979	21 31 24.9	41.9N	130.9E	566	5.8	74.6	42
04	24	08	1979	04 26 54.5	9.0N	83.5W	43	5.2	86.3	279
05	24	08	1979	16 59 28.9	41.2N	108.1E	18	5.6	63.8	56
06	27	05	1980	14 51 00.3	37.5N	118.8W	22	5.7	82.6	322
07	05	07	1980	20 25 25.2	41.9N	77.4E	22	5.4	45.5	74
08	22	01	1981	19 34 43.0	38.3N	142.7E	35	6.1	82.6	37
09	04	09	1981	11 15 13.9	9.9N	124.0E	651	6.0	96.8	66
10	12	09	1981	07 15 53.8	35.7N	73.6E	30	6.2	46.6	83
11	25	10	1981	03 22 16.0	18.2N	102.0E	28	6.2	90.4	299
12	01	07	1982	07 41 53.7	51.4N	179.9W	51	6.3	78.8	7
13	04	07	1982	01 20 08.2	27.9N	137.0E	554	6.2	88.9	46
14	31	07	1982	06 29 13.2	51.8N	176.1E	18	6.2	78.1	10
15	24	01	1983	23 09 21.7	12.9N	93.6E	81	6.1	75.4	87
16	14	02	1983	08 10 04.3	55.0N	159.2W	37	6.0	75.4	354
17	01	05	1983	18 10 40.7	46.4N	153.4E	24	6.1	78.9	26
18	02	05	1983	23 42 37.7	36.2N	120.3W	7	6.2	84.3	323
19	02	06	1983	20 12 50.9	9.5S	71.2W	600	5.8	92.4	258
20	09	06	1983	12 49 02.7	40.3N	139.0E	22	6.3	79.4	38
21	09	06	1983	18 46 04.2	51.4N	174.1W	46	6.1	79.2	356
22	10	06	1983	02 13 23.2	75.5N	127,8E	10	5.5	48.5	18
23	21	06	1983	14 48 07.9	24.1N	122.4E	43	5.8	84.5	51
24	24	06	1983	07 18 22.3	21.8N	103.3E	18	6.0	75.2	74
25	24	06	1983	09 06 46.3	24.2N	122.4E	48	6.0	84.5	51
26	28	06	1983	03 25 16.7	60.2N	141.3W	14	5.9	68.2	346
27	07	07	1983	20 35 37.4	7.4S	27.9E	10	5.8	58.5	161
28	26	10	1984	20 22 21.8	39.2N	71.3E	33	6.0	43.1	80
29	01	05	1985	13 27 56.1	9.2S	71.2W	600	6.0	92.4	258
30	06	05	1985	03 04 22.7	30.9N	70.3E	37	5.6	47.5	90
31	14	05	1985	13 24 57.8	10.6S	41.4E	10	6.0	65.6	147
32	14	05	1985	18 11 08.9	10.5S	41.4E	10	6.4	65.6	147
33	16	05	1985	14 20 25.1	29.1S	77.7E	10	5.9	98.1	126
34	06	06	1985	02 40 12.9	0.9N	28.4W	10	6.3	59.2	227
35	26	04	1986	07 35 16.0	32.1N	76.3E	33	5.5	50.6	85
36	06	07	1986	19 24 26.3	34.4N	80.1E	33	5.8	51.6	80

the distribution of events within this range were nearly the same for each group. No attention was paid to the azimuths of events. The results for the first and second frequency band are presented in Fig. 9. A comparison shows that the times and amplitudes of the second phase (at 68.2 s) are nearly the same in the two groups. This result coincides with that obtained in a similar experiment with NORSAR data (Vinnik et al., 1983) and attests the estimates of the times and amplitudes of the converted phases as highly accurate. On the other hand, the appearance of the first phase (at 45.0 s) is rather different in the two groups. The difference is mainly in the frequency content, which is especially clear in the broad frequency band.

In another experiment, the events were divided into groups according to their azimuth. The first group assembled was of the events with an azimuth between 75° and 345°; the second group included all other events. Most of the available events are located to the east of the array. For this reason, the results for the first group correspond mainly to the east and south-east, while those for the second group are characteristic of the north and north-east. In the two groups, the amplitude of the second phase is nearly the same, while those of the first one are strongly different (Fig. 10). The difference is especially pronounced in the frequency band around 0.1 Hz, where the first phase is either absent (Fig. 10d) or very strong and clear (Fig. 10c). This could indicate that the conversion at 400 km depth depends strongly on the azimuth.

Fitting the crustal data

The initial part of the summed $\hat{H}$-component records was used to infer the structure of the crust underneath the array. A similar method using unrotated and undelayed, but normalized and stacked records of teleseismic P waves was used by Owens et al. (1987) to derive the crustal structure underneath the RSTN stations in North America.

Figure 11 shows the comparison of undelayed summed $\hat{H}$ components of observed and theoretical traces. These data are mainly sensitive to the structure of the crust, the curst-mantle boundary and the uppermost part of the mantle. Superimposed on each other are the observed displacement data from Figs. 8–10 for different subsets of events and for zero conversion depth. We have also added two more groups of events, where the data have been split by magnitude (larger or smaller than 6.0). The differences between the different data traces are indications of the reliability of the data. These differences are small compared to the amplitudes of the signal. This shows that we have stable information about the crust, which is independent of the

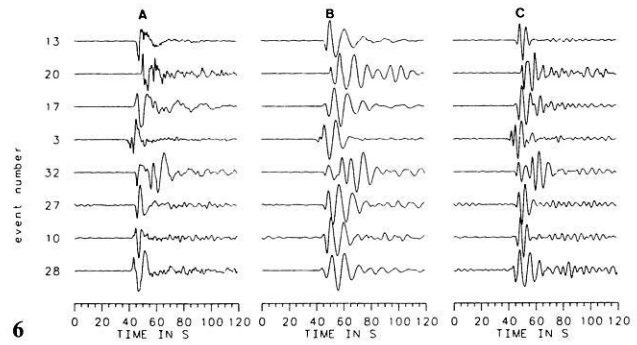

6

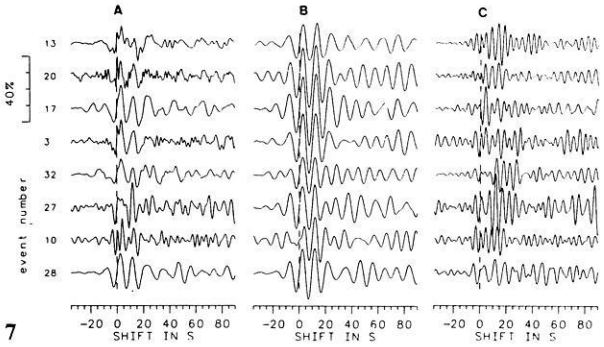

7

Fig. 6. Normalized vertical components of examples of records used in this study. The numbers on the left refer to the event numbers in Table 1. The seismograms labelled *A*, *B* and *C* are for displacement and bandpasses around 0.1 and 0.2 Hz, respectively

Fig. 7. $\hat{H}$ components for the same earthquakes and filters as in Fig. 6

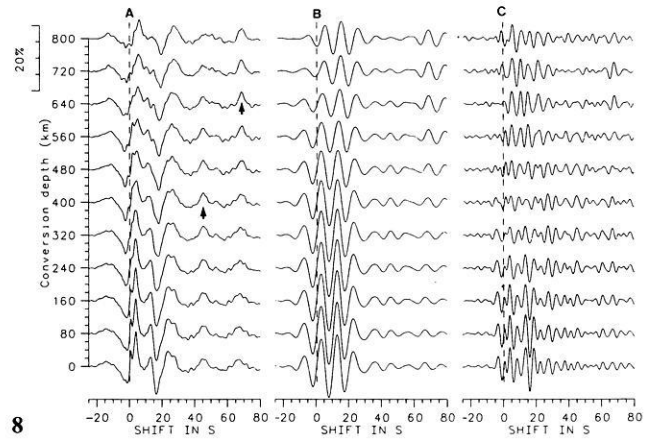

8

Fig. 8. Delayed and summed $\hat{H}$ components for the same filters as in Figs. 6 and 7, and for all usable events. The delays from Fig. 2 are used for a number of trial conversion depths. At conversion depths near 400 and 640 km, the phases corresponding to the times around 45 and 68 s have their largest amplitudes (see *arrows*). These are the upper-mantle converted phases

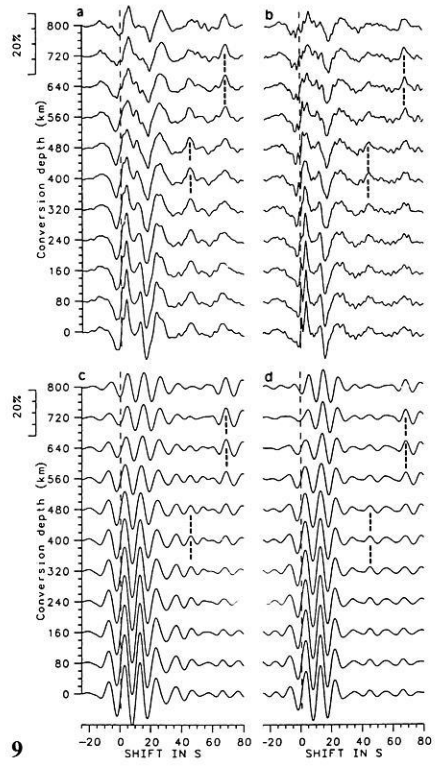

9

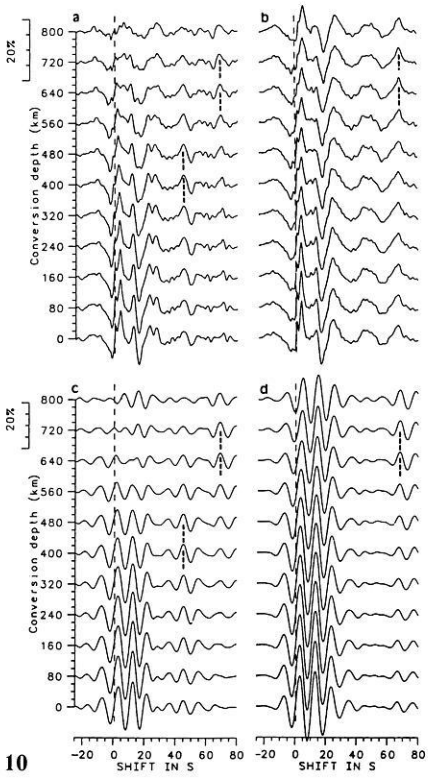

10

Fig. 9a–d. Delayed and summed $\hat{H}$ components for two sub-groups of events [displacement (**a**, **b**), and 0.1-Hz bandpass filter (**c**, **d**)]. All distances are evenly distributed on both groups, the azimuth is disregarded. The marked converted phases do not vary significantly with the group

Fig. 10a–d. Delayed and summed $\hat{H}$ components for two other sub-groups of events, same filters as in Fig. 9. The first group (**a** and **c**) contains all events between 75° and 345° azimuth. The second (**b** and **d**) contains the rest of the events. The conversion at the 400-km discontinuity (near 45 s) depends strongly on azimuth

subset of events. Since we have used summed records of the three-component stations of the GRF array, these data only provide information about the average structure of the area of the array. The same method applied to the individual stations of the array could possibly resolve differences in the crustal structure between the stations. Traces A–E in Fig. 11 are theoretical traces for different crustal models after the same data processing which was used for the observed data. All traces are on the same amplitude scale, so that the amplitudes can be compared directly. The

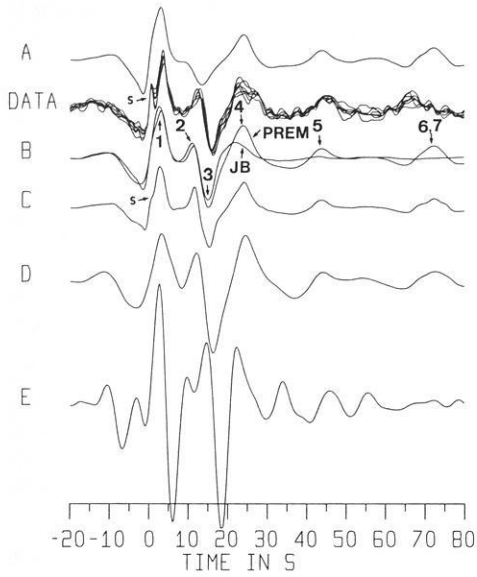

Fig. 11. Comparison of theoretical and observed $\hat{H}$ functions. The displacement traces from Figs. 8–10 for zero delay are superimposed on each other in the DATA trace. The crustal models for the theoretical traces *A*, *B*, *D* and *E* are given in Table 2; the mantle model is PREM, except for the trace labelled *JB*. The rise time of the source function is 4.5 s, except for trace *C*, where it is 1.5 s; the crustal model for this trace is model B. The labelled phases are the same as in Figs. 3 and 4. Phase *s* is the conversion at the bottom of the sediments

Table 2. Curstal models used for the computation of theoretical seismograms in Fig. 11. Left column is depth in km, right column is *P* velocity in km/s. The *P*-to-*S* velocity ratio is 1.8 for models A and B, and 1.73 for models D and E

Model A		Model B		Model D		Model E	
0.0	5.00	0.0	5.00	0.00	2.00	0.0	3.00
0.2	5.00	0.2	5.00	0.83	5.60	4.0	3.00
0.2	2.50	0.2	2.50	2.50	5.80	4.0	6.00
0.8	2.50	0.8	2.50	4.58	5.95	30.0	6.00
0.8	5.80	0.8	5.80	4.58	5.70	30.0	8.11
30.0	8.11	30.0	7.90	12.50	5.70		
		30.0	8.11	15.00	6.30		
				20.00	6.40		
				24.20	6.90		
				30.00	7.20		
				30.00	8.11		

P velocities of the models used in Fig. 11 are given in Table 2. The assumed *P*-to-*S* velocity ratio is 1.8 for models A and B, and 1.73 for models D and E. The density derived from Birch's law was used. Note the thin low-velocity layers in models A and B underneath the high-velocity top layer, as mentioned before. The PREM upper-mantle model is used in most cases; only in traces B is the Jeffreys-Bullen model also used for comparison. The rise time used for all traces except C is 4.5 s. Trace C is computed for model B, but a rise time of 1.5 s is used. Trace C contains higher frequencies, which makes the conversion at the bottom of the sediments more easily visible. This theoretical conversion is still not strong enough compared with the observed one.

The data traces in Fig. 11 are in good agreement with each other up to about 20 s after zero time (which is the *P* arrival time). After that, the scatter increases. The numbered phases 1–7 in trace B are the same phases as in Figs. 3 and 4. The phase labelled "*s*" is the conversion at the sediments. It seems astonishing that even this phase can be seen in the observed and theoretical (trace C), rather long-period data. It is clearly larger in the observed data than in the theoretical ones. But we are not trying to interpret this phase, since we are using summed data of three stations, and the sediments are different at each station. The signal forms and amplitudes of phases 1, 2 and 3 (the conversion at the Moho, the *PS* and *SS* multiples in the crust) in trace B are in very good agreement with the data. Models A and B are very similar. Their main difference is that the velocity jump at the Moho varies; and also the average gradient in the crust varies somewhat, but this is less important. Model A has no first-order discontinuity at the Moho at all, and model B has a *P*-velocity jump of 0.2 km/s there. The traces belonging to these models vary mainly in the amplitudes of phases 2 and 3. Although model A has no first-order discontinuity at the Moho, it is still able to produce relatively strong converted energy in the frequency range used.

Model D was obtained by Aichele (1976) from refraction studies near the GRF array. The general agreement of trace D with the data is fairly good, but multiples 2 and 3 are clearly too strong. The jump in *P* velocity of 0.9 km/s at the Moho is responsible for that.

A hypothetical model E, consisting of a homogeneous crust with a homogeneous sedimentary layer on top, is in complete disagreement with the data. Not only do the signal forms disagree but, also, the amplitudes of the converted crustal shear waves are much too large. Such types of models with strong discontinuities produce far too much converted and multiply reflected shear energy. The crustal reverberations of model E continue for a long time, which would make it impossible to observe conversions from upper-mantle discontinuities.

Phase 4 in the theoretical traces in Fig. 11 is the conversion at the 220-km discontinuity of the PREM model. For comparison, the Jeffreys-Bullen model has also been put underneath the crustal model of trace B. There is much energy in the data trace at this time, which is above the level predicted by the JB model. PREM is closer to the data than JB. We conclude from this that there possibly exists underneath the GRF array, at about 220 km depth, a discontinuity which, at a first approximation, is similar to that in PREM. A special effort is required in the future to add more details to the description of this discontinuity.

Phases 5 and 6 are the conversions at the 400- and 670-km discontinuities. Here and later we label the discontinuities as 400-km and 670-km discontinuities without implying that their real depths are 400 and 670 km. These phases are not very clear in Fig. 11 because the appropriate delays have not been used in this figure. This well be done next. The appropriate delays ogf the 200-km discontinuity have also not been used in Fig. 11, but this is less severe as Fig. 4 shows.

The upper-mantle discontinuities

Figure 12 shows the converted phases from both upper-mantle discontinuities. The 0.1-Hz filter is called LP in this figure, and the 0.2-Hz is called SP. The top traces are the displacement data. The SP data are computed for all usable

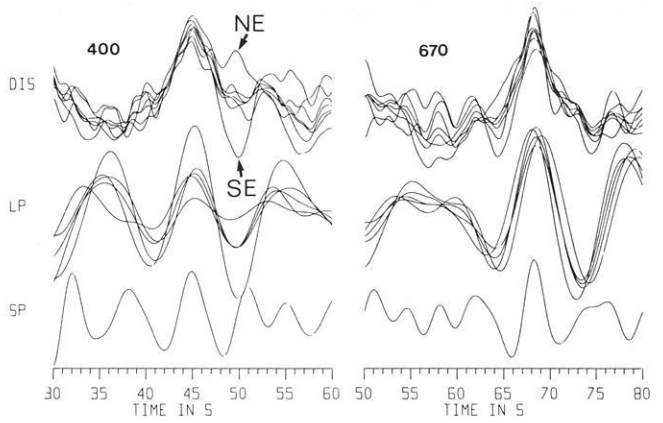

Fig. 12. Superposition of all mantle conversion data. Summation delays correspond to the 400- and 670-km conversion depths. *DIS*, *LP* and *SP* are displacement, 0.1- and 0.2-Hz filters. The records for different event azimuths (*NE*, *SE*) are strongly different at times around 49 s. All data are on the same amplitude scale

events, and the LP traces are computed for all events and the groups of events shown in Figs. 9 and 10. The displacement traces are shown for the same groups of events as the LP traces and, in addition, two groups are formed by dividing the events by magnitude (smaller and greater than 6.0). The largest difference between the traces is observed at about 49 s, when the data are divided according to the event azimuth. This could be due to a lateral heterogeneity of the 400-km transition in the vicinity of the array. The signal-to-noise ratio in the SP band is low for the 400-km conversion and fairly high for the 670-km phase.

In Fig. 13 we compare the signals from the Moho, the 400- and the 670-km discontinuities in the displacement records. The Moho data are plotted on a scale 3 times smaller than the upper-mantle data. Now we can compare directly the signal forms of the three different conversions. In Fig. 14, the converted phases from Fig. 13 are normalized to roughly the same maximum of the group containing all usable events. In addition, Fig. 14 shows the sum of the autocorrelation functions of the *P* wave of all events, normalized to the same maximum. Figures 13 and 14 demonstrate that the autocorrelation function of *P*, the conversion at the Moho and the 670-km conversion have a similar form (the conversion at the bottom of the sediments seen at the beginning of the Moho conversion must not be considered in this connection). The conversion at 400 km is about 1 s broader than the other signals. These observations imply that the sharpness of the 670-km discontinuity is comparable with that of the crust-mantle transition, while the 400-km discontinuity is less sharp than the other two. The reader should have in mind here that the crust-mantle transition includes not only the Moho boundary but the lower crust as well.

Since we want to compare theoretical and observed signal forms, the question of what rise times should be used for the computation of the theoretical seismograms is very important. For this purpose we matched theoretical and observed sums of autocorrelation functions of *P* waves. The theoretical data were summed up to 80° distance. If we use records from larger distances, then the broadening of the *P* signal at these distances contaminates the results. About two-thirds of our observed events are from distances shorter than 80°. As a test, we have summed only these events and found good agreement with all other groups. The bottom traces in Fig. 15 shows the comparison of the autocorrelation functions of the theoretical and observed *P* signal. Good agreement is obtained with a rise time of 4.5 s. Now we can use this rise time for the theoretical seismograms and compare the theoretical conversions for the PREM model with the observed ones. We obtain from Fig. 15 the following clear results: the 400-km signal of PREM comes about 2 s earlier than the observed one at GRF; the 670-km signal of PREM is about 1 s later than the observed GRF signal. The amplitude of the 400-km signal of PREM is about 30% smaller than in the GRF data; the amplitude of the 670-km signal of PREM is in agreement with the GRF data. The PREM model clearly needs some adjustments to fit the GRF data.

In Fig. 16 we compare the observed upper-mantle signals with theoretical data for modifications of PREM. In the modification M of PREM, the 400-km discontinuity is moved to 417 km depth and the *P*- and *S*-velocity and density contrasts have been increased by 50%. The 670-km discontinuity is moved to 660 km depth, without any other change. The theoretical data for M agree reasonably well with our observations. In the modification MG of M, the first-order discontinuities of M are replaced by 20-km-thick gradient zones. As expected, the amplitudes of the conversions are reduced, but the signal is not broadened much. An increase in the contrast could again fit the amplitudes.

It should be noted that lateral velocity variations in the lithosphere-asthenosphere system are quite sufficient to account for the 2-s delay of the 400-km phase in the GRF data with respect to PREM. For this reason, the 417-km depth of this discontinuity in the M and MG models must be regarded as an arbitrary value. Similarly, velocity variations in the lithosphere and asthenosphere will affect the time of the 670-km phase. On the other hand, the lateral velocity variations in the 400–700 km depth range are less significant, which makes the value of the depth interval between the two discontinuities in M and MG (243 km) fairly reliable. This value is about 30 km less than in PREM.

Conclusions

The data-processing method used has facilitated the detection of weak phases in noisy data. Relatively clear *P*-to-*S* converted phases with amplitudes less than 4% of the *P*-wave amplitude have been extracted from the coda of *P* phases. These observations throw new light on the fine *S*-velocity structure of the mantle discontinuities.

The same method has been applied by Vinnik et al. (1983) to the records of a few other stations. The observed times of the conversions from their paper and from the present study are (in seconds):

Station	$t_{Ps}(400)$	$t_{Ps}(670)$	$t_{Ps}(670)-t_{Ps}(400)$
TUC	47.5	70.1	22.6
GOL	46.3	69.8	23.5
NORSAR	44.5	68.0	23.5
Obninsk	43.2	66.7	23.5
GRF	45.0	68.2	23.2
PREM			26.0

These values are valid for a reference slowness of 6.4 s/degree (or 67° distance). The difference between the times

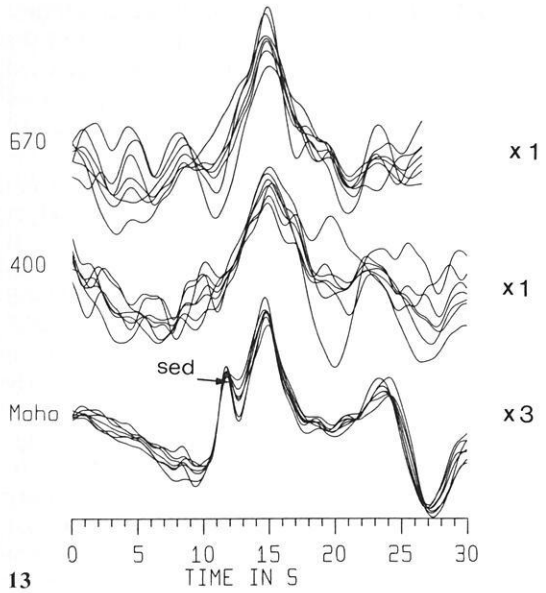

13

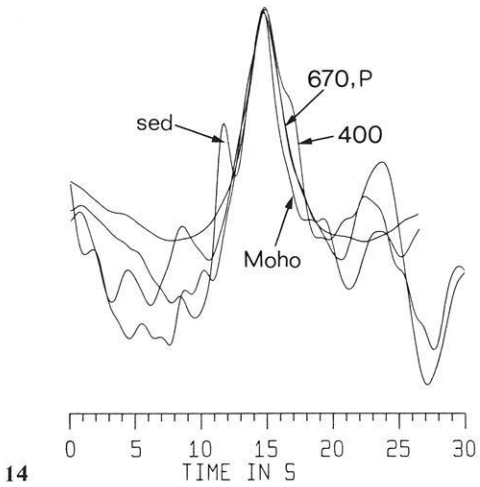

14

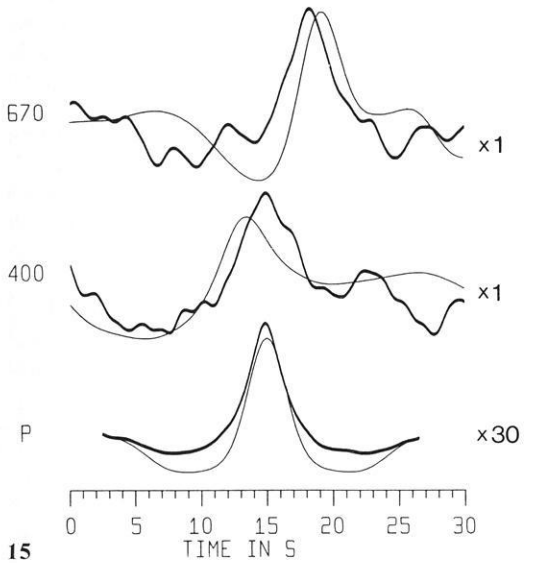

15

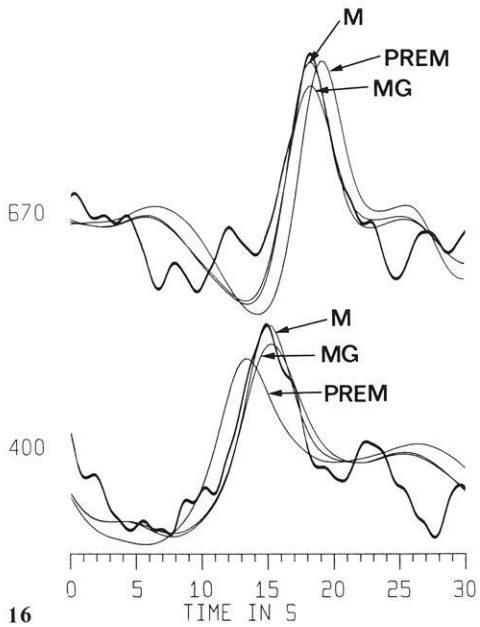

16

Fig. 13. Wave-form comparison of the conversions at the Moho and the upper-mantle discontinuities (displacement). The Moho conversion was reduced by a factor of 3. The conversion at the sediments is marked "*sed*"

Fig. 14. Wave-form comparison of the same conversions as in Fig. 13. Only the summation of all usable events is used. The amplitudes are normalized to the same maximum. The autocorrelation function of the *P* wave, summed over all events, is shown in addition. Figure 12 and this figure indicate that all wave forms are fairly similar, except the conversion at 400 km depth. This signal is about 1 s broader than the others

Fig. 15. Comparison of wave forms of the observed (*heavy lines*) and computed (*light lines*) upper-mantle conversions and the autocorrelation function of the *P* signal for the PREM model. A rise time of 4.5 s is used for the theoretical seismograms, which fits the observed autocorrelation of the *P* signal best. The amplitudes of the *P* traces have been reduced by a factor of 30

Fig. 16. Fit of observed and computed mantle conversions (displacement). Model *M* is a modification of PREM, where the 400-km discontinuity is moved to 417 km and its contrast is increased by 50%; the 670-km discontinuity is moved to 660 km. In model *MG*, the first-order discontinuities of M are replaced by 20-km-thick gradient zones. All traces are on the same amplitude scale

of the two recorded phases is remakably stable: the average of the data for TUC, GOL, NORSAR and Obninsk is equal to the result for GRF. This difference is 2.8 s less than for PREM. It follows that the depth interval between the two discontinuities in PREM is biased by about 30 km. According to Vinnik et al. (1983) the error is, most likely, in the depth of the 670-km discontinuity.

Our data can also provide important constraints on the fine velocity structure of the 670-km transition. The amplitudes of the 670-km phase are different in different frequency bands (see Fig. 12). This would be impossible if the 670-km transition were a first-order discontinuity. Also, a complex structure is found near 400 km depth. The spectral content of the 400-km phase is clearly different in the

groups of events which are assembled according to their azimuth (Fig. 12). An accurate description of the corresponding fine structure of both discontinuities is difficult; therefore, we postpone attempts to do this until additional data have been accumulated. Processing of single-station records of the array seems to be especially promising in this respect.

In general, the method has proved to be very useful for detailed mapping of the fine structure of the upper mantle. High-quality data (especially broadband data) are necessary for its application. It is also extremely sensitive to crustal structure. Therefore, the method can be recommended for future applications in this broad field of research.

Finally we suggest that the method could also be applied to other weak phases, e.g. to *PcP* and to forerunners of *S* or *PP*.

Acknowledgements. This research has been made possible by the agreement between the Academy of Sciences of the USSR and the Deutsche Forschungsgemeinschaft. We wish to thank Winfried Hanka for help in the computations, and Gerhard Müller and Jörg Schlittenhardt for reading the manuscript.

References

Aichele, H.: Interpretation refraktionsseismischer Messungen im Gebiet des Fränkisch-Schwäbischen Jura. Dissertation, Universität Stuttgart, 1976

Dziewonski, A.M., Anderson, D.L.: Preliminary reference Earth model. Phys. Earth Planet. Inter. **25**, 297–356, 1981

Faber, S., Müller, G.: Converted phases from the mantle transition zone observed at European stations. J. Geophys. **54**, 183–194, 1984

Jeanloz, R., Thompson, A.B.: Phase transitions and mantle discontinuities. Rev. Geophys. Space Phys. **21**, 51–74, 1983

Kind, R.: The reflectivity method for different source and receiver structures and comparison with GRF data. J. Geophys. **58**, 146–152, 1985

Liu Qiyuan, Kind, R.: Lateral variations of the structure of the crust-mantle boundary from conversions of teleseismic P waves. J. Geophys. **60**, 149–156, 1986

Owens, T.J., Taylor, S.R., Zandt, G.: Crustal structure at regional seismic test network stations determined from inversion of broadband teleseismic P waveforms. Bull. Seismol. Soc. Am. **77**, 631–662, 1987

Paulssen, H.: Upper mantle converted waves beneath the NARS array. Geophys. Res. Lett. **12**, 709–712, 1985

Schlittenhardt, J.: Investigation of the velocity and Q structure of the lowermost mantle using PcP/P amplitude ratios at distances of 70°–84°. J. Geophys. **60**, 1–18, 1986

Vinnik, L.P.: Detection of waves converted from P to SV in the mantle. Phys. Earth Planet. Inter. **15**, 39–45, 1977

Vinnik, L.P., Avetisjan, R.A., Mikhailova, N.G.: Heterogeneities in the mantle transition zone from observations of P-to-SV converted waves. Phys. Earth Planet. Inter. **33**, 149–163, 1983

Received July 30, 1987; revised version October 2, 1987
Accepted October 2, 1987